Revision 1

The vibrational features of hydroxylapatite and type A carbonated apatite: a first principle contribution.

Gianfranco Ulian[1], Giovanni Valdrè[1,]*, Marta Corno[2] and Piero Ugliengo[2]

[1]*Dipartimento di Scienze della Terra e Geologico-Ambientali*
Centro di Ricerche Interdisciplinari di Biomineralogia, Cristallografia e Biomateriali,
Università di Bologna "Alma Mater Studiorum" Piazza di Porta San Donato 1, Bologna, Italy.
E-mail: giovanni.valdre@unibo.it
[2]*Dipartimento di Chimica, NIS Centre of Excellence and INSTM (Materials Science and Technology) National Consortium, UdR Torino, Via P. Giuria 7, Torino, Italy.*

Abstract

In this work, the vibrational spectra of hexagonal hydroxylapatite OHAp (space group $P6_3$) and type A carbonated apatite [$Ca_{10}(PO_4)_6(CO_3)$, space group P1] have been calculated with an *ab initio* approach by density function method using the hybrid B3LYP functional and an all-electron polarized double-zeta quality Gaussian-type basis set using CRYSTAL09 computer program. The effect on the vibrational properties due to improving the Ca pseudopotential, usually adopted in previous studies on hydroxylapatite, towards the present all-electron basis set has also been briefly addressed. The anharmonic correction for hydroxyl groups in OHAp has also been considered. The results of the modeling are in good agreement with the available FTIR and Raman data present in literature and can be useful to experimental researchers to assign unequivocally the bands in infrared and Raman spectra to specific fundamental vibrational modes.

Keywords: hydroxylapatite, type A carbonated apatite, IR, vibrational properties, *ab initio* quantum mechanics, DFT

INTRODUCTION

Apatite minerals are an important group of minerals not only because they are commonly found in almost all type of rocks, but also because carbonate hydroxylapatite COHAp is the main component of the mineral phase of mammalian bones (Dorozhkin, 2009; Dorozhkin, 2010). The two natural polymorphs of hydroxylapatite are monoclinic [$P2_1/b$] and hexagonal [$P6_3/m$] and can be found mainly in minerals and bone tissues, respectively. At standard temperature and pressure,

the monoclinic cell is more stable than the hexagonal one; the phase transition between the two polymorphs (order/disorder) takes place at 200°C. Nevertheless, the hexagonal OHAp allows extensive atomic substitution and non-stoichiometry in Ca, P and channel anion positions to entropically stabilize its structure (Suda et al., 1995). For example, anions such as fluoride, chloride and carbonate can easily enter in the *c*-axis channel, leading to fluoro-, chloro- and carbonate apatites, both as end-members and in mutual solid solutions (Elliott, 1998; Hughes and Rakovan, 2002).

The carbonate ion substitution in hydroxylapatite has been extensively studied, because the CO_3^{2-} ion is commonly present in natural bone tissues in substantial amount (about 4-6 wt. %). As a consequence, the inclusion of carbonate ion in apatite-based biomaterial could increase the biocompatibility of implanted prosthetic.

Carbonate ion can substitute for both OH in the *c*-axis channel of apatite (type A) and the phosphate group (type B), as already described by many authors (Astala and Stott, 2005; Fleet and Liu, 2007; Fleet and Liu, 2008; Fleet and Liu, 2003; Fleet and Liu, 2004; Fleet et al., 2004; Fleet et al., 2011; Kovaleva et al., 2009; Sturgeon and Brown, 2009). In a very recent paper, Ulian and co-workers (2012) modelled the structures of both OHAp and type A carbonated apatite (CAp) by periodic *ab initio* simulation with DFT/B3LYP hybrid functional and with an all electron Gaussian basis set for all the atoms in the unit-cell. Figures 1a and 1b report the optimized crystallographic cells of OHAp and CAp, respectively. They found that the carbonate ion is preferably oriented in the Ca^{2+} channel in a "closed" configuration (type A1 CAp), with a bisector of the CO_3^{2-} triangle perpendicular to the *c*-axis. This result was in agreement with both single crystal X-Ray Diffraction (XRD) data (Fleet and Liu, 2003; Fleet et al., 2011) and previous theoretical results (Peroos et al., 2006). However, the simulation with DFT/B3LYP hybrid functional with an all electron gaussian basis set for all the atoms in the unit cells of OHAp and CAp provided the closest structures to the experimental derived ones.

Alongside single-crystal XRD, two of the most employed tools to experimentally investigate the internal structure of a solid phase are Fourier-Transformed InfraRed (FTIR) and Raman spectroscopy. These techniques resolve specific vibrational mode of the different molecular groups in the sample and they have been extensively used for the characterization of both OHAp (Bertinetti et al., 2007; Cuscó et al., 1998; Miller et al., 2001; Tsuda and Arends, 1994) and carbonated hydroxylapatite (COHAp) (Fleet, 2009; Fleet and Liu, 2008; Fleet and Liu, 2003; Fleet and Liu, 2004; Fleet et al., 2004; Petra et al., 2005; Suetsugu et al., 1998). From the position of the IR/Raman signals it is possible to obtain information on the chemical environment of each molecular group in the mineral. The most important IR vibrational mode in carbonated apatite is the CO_3^{2-} out-of-plane bending (labelled as ν_2). This vibrational mode falls at slightly different wavenumbers depending on the site (A or B) occupied by the carbonate ion in the apatite cell. From the relative intensities of the $\nu_2(CO_3)$ peaks it is possible to evaluate the relative amount of A and B sites in the sample (Fleet, 2009; Kolmas et al., 2011; Petra et al., 2005).

However, the interpretation of experimental vibrational spectra of both natural and synthetic samples can be complicated by several factors, for instance: (1) the presence of impurities from preliminary treatments and the synthesis process of the sample; (2) the nature and the morphology of the samples (powders or single crystals); (3) the presence of overtones and/or combination peaks, and (4) band broadening and overlap of signals.

One of the most reliable solution to overcome the problems cited above is the quantum mechanical simulation of the vibrational spectrum of the sample of interest. This approach was effectively adopted by many researchers in their theoretical investigations of the vibrational properties of hydroxylapatite, α-quartz, brucite, magnesite, calcite and dolomite (Corno et al., 2006; Pascale et al., 2004; Prencipe et al., 2004; Ugliengo et al., 2004; Valenzano et al., 2007; Valenzano et al., 2006). Furthermore, the comparison between the computed vibrational spectra with the experimental ones is another way to validate the chosen modelling method, other than to compare the modelled structures with those obtained by XRD.

The aim of the present work is to provide the simulated vibrational spectra of both OHAp and type A1 CAp, using the optimized geometries previously evaluated with DFT/B3LYP level of theory and a complete basis set for each atom in the structures (Ulian et al., 2012). The results from this kind of calculation can be used to unequivocally assign each signal to specific normal modes and can help the experimental researchers in identifying which bands in their spectra correspond to fundamental vibrational transitions.

COMPUTATIONAL DETAILS

All calculations have been performed on a Debian (Linux) Cluster with the *ab initio* CRYSTAL09 code (Dovesi et al., 2009), which implements the Hartree–Fock and Kohn–Sham self consistent field method for the study of periodic systems. The graphical drawings have been carried out with the molecular graphics program VESTA (Momma and Izumi, 2008). The analysis of the vibrational modes were made with MOLDRAW (Ugliengo, 2009).

Basis set

Multielectron wave functions are described by linear combination of crystalline orbitals (CO), expanded in terms of Gaussian-type basis sets. For all the calculations, calcium has been described with a 86-511G(2d), used by other authors for calcite (Valenzano et al., 2006), with outer shell exponents α_{sp} = 0.453 bohr^{-2}, α_{d1} = 3.1910 and 0.8683 bohr^{-2} and α_{d2} = 0.2891 bohr^{-2}. The phosphorus atom is described by the basis 85-21G(d), α_{sp} = 0.48105 and 0.135 bohr^{-2} and α_{d} = 0.74583 bohr^{-2}, respectively. Oxygen and hydrogen are both represented by a 6-31G* basis set with the outer shell exponents α_{sp} = 0.2742 bohr^{-2} and α_{d} = 0.538 bohr^{-2}; and α_{sp} = 0.1613 and α_{p} = 1.1 bohr^{-2}, respectively. Finally, the carbon atom is described by a 6-21G* basis set with α_{sp} = 0.26 bohr^{-2} and α_{d} = 0.8 bohr^{-2}.

Hamiltonian and computational parameters

The Becke three-parameter (B3LYP) hybrid exchange functional (Becke, 1993) in combination with the gradient-corrected correlation functional of Lee, Yang, and Parr (Lee et al., 1988) has been adopted for all calculations. This functional has been already used for alkali oxides, α-quartz, calcite and hydroxylapatite (Dovesi et al., 1991; Pascale et al., 2004; Prencipe et al., 2004). The presence of some fraction of exact exchange increases the electronic localisation, which in turn increases the ionic nature of the materials, causing a systematic decrease of the lattice parameters and an increase of the elastic constants and bulk moduli. The exchange–correlation contribution is performed over a grid of points and is the result of a numerical integration of the electron density and its gradient. The adopted pruned grid is given by 75 points and 974 angular points, subdivided into 5 sub-intervals of 86, 194, 350, 974 and 350 points and obtained from the Gauss–Legendre quadrature and Lebedev schemes (Prencipe et al., 2004). This is a good compromise between accuracy and cost of calculation for geometry optimization and vibrational frequencies. The values of the tolerances that control the Coulomb and exchange series are the default provided by CRYSTAL09 (*ITOL1* to *ITOL4* = 6) (Dovesi et al., 2009), but we increased the pseudo-overlap parameter (*ITOL5*) from 12 to 14. The Hamiltonian matrix has been diagonalized (Monkhorst and Pack, 1976) using a shrinking factor of *IS* = 4 (Dovesi et al., 2009), that leads to 12 and 36 reciprocal lattice points (k-points) for OHAp and CAp, respectively.

Geometry

The cell parameters and fractional coordinates were optimized by the analytical gradient method in a recent work, adopting the same computational condition explained above (Ulian et al., 2012). Here we report a summary of the results in Table 1 for hydroxylapatite and type A1 carbonated apatite (CAp). For complete details, we suggest the reader to refer to the above referenced paper.

Vibrational features

In periodic systems and within the harmonic approximation, the phonon frequencies at Γ point are evaluated diagonalising the central zone ($k = 0$) mass-weighted Hessian matrix:

$$W_{ij}(k=0) = \sum_G \frac{H_{ij}^{0G}}{\sqrt{M_i M_j}}$$

H_{ij}^{0G} is the second derivative of the electronic and nuclear repulsion energy E evaluated at equilibrium **u=0** with respect to the displacement of atom A in cell 0 ($u_i = x_i - x_i^*$) and displacement of atom B in cell G ($u_j = x_j - x_j^*$) from their equilibrium position x_i^*, x_j^*:

$$\sum_G H_{ij}^{0G} = \sum_G \left[\frac{\partial^2 E}{\partial u_i^0 \partial u_j^G} \right]_0 \qquad i = 1,...,3N; \quad j = 1,...,3N$$

In CRYSTAL, the calculation of the Hessian at equilibrium is made by the analytical evaluation of the energy first derivatives, Φ_j of E with respect to the atomic displacements:

$$\Phi_j = \sum_G v_j^G = \sum_G \frac{\partial E}{\partial u_j^G} \qquad j = 1,...,3N$$

while second derivatives at **u = 0** (where all first derivatives are zero) are calculated numerically using a "two-point" formula:

$$\left[\frac{\partial \Phi_j}{\partial u_i^0} \right]_0 \approx \frac{\Phi_j(0,...,u_i^0,...,0) - \Phi_j(0,...,u_i^0,...,0)}{u_i^0} \qquad i = 1,...,3N; \quad j = 1,...,3N$$

More details on the vibrational calculation made by CRYSTAL can be found in literature (Pascale et al., 2004; Tosoni et al., 2005). The Hessian matrix eigenvalues provide the normal harmonic frequencies ω_n and it is obtained with 3N+1 SCF and gradient calculation. This method can be quite demanding for large unit cells, but point symmetry facilitates a remarkable time saving, because only the lines of the Hessian matrix referring to irreducible atoms need to be generated.

In addition, an anharmonic correction has been applied to the OH stretching mode in the OHAp cell. This three-step procedure is based on: (i) decoupling of the distance O–H, which is treated as a pure normal coordinate; (ii) calculation of the total energy of the system for a set of OH values around equilibrium (0.2/+0.3Å), followed by an interpolation by means of a sixth-order polynomial fit, and (iii) solution of the one-dimensional nuclear Schrödinger equation to obtain the three lowest eigenvalues, E_0, E_1 and E_2, from which one can calculate the fundamental frequency $\omega_{01} = E_1 - E_0$, the first overtone $\omega_{02} = E_2 - E_0$ and the anharmonicity constant of the OH mode, $\omega_e\chi_e = (2\,\omega_{01} - \omega_{02})/2$. This algorithm was proposed by Lindberg (1988) and already adopted by other authors (Pascale et al., 2004; Ugliengo et al., 2004; Ulian et al., 2012).

RESULTS AND DISCUSSION

Both hydroxyl- and carbonated apatite cells have 44 atoms and 44 x 3 = 132 associated degrees of freedom, of which 129 have vibrational character. The analysis of the vibrational modes has been conducted with the aid of (i) the visualization software MOLDRAW and (ii) the potential energy distribution (PED) computed by CRYSTAL09. These methodologies provide data that are particular useful to individuate different IR regions in the spectra, in particular for the phosphate ion vibrational bands.

Hydroxylapatite

Corno and co-workers (Corno et al., 2006) made a complete analysis of the vibrational modes for their OHAp model simulated with an all electron basis set except for the pseudopotential on the calcium atoms. In our simulations we followed their approach, but we used a complete all electron basis set for all the atoms of the OHAp cell. We compared our results with the experimental IR and Raman spectra present in literature.

In the OHAp structure the $P6_3$ symmetry subdivides the 132 vibrational modes in the different following irreducible representations:

$$\Gamma_{total} = 22A + 22B + 22E_1 + 22E_2$$

66 of these modes are active in the IR ($22A + 22E_1$) and 110 are active in Raman ($22A + 22E_1 + 22E_2$). The 22 B-symmetry modes are silent in both IR and Raman. The first A and E1 modes are associated with 3 acoustic (translation) modes and were not considered.

In Figure 2 we report the simulated infra-red vibrational spectrum of hydroxylapatite from 0 to 1300 cm^{-1}.

The lowest energy signals (100-400 cm^{-1}) are phonon modes, related to vibrations of the crystal lattice. The range from 500 to 1200 cm^{-1} in the spectra was mainly given by PO_4^{3-} ions bands. As already discussed by Corno et al. (2006), Cuscó et al. (1998), Rehman and Bonfield (1997), Tsuda and Arends (1994), the free phosphate tetrahedron in aqueous solution gives four vibrational modes (irreducible representations A_1+E+2F): (i) the symmetric P-O stretching (ν_1, A_1) at 938 cm^{-1}; (ii) the symmetric OPO bending (ν_2, E) at 420 cm^{-1}, which are IR inactive; (iii) the asymmetric P-O stretching (ν_3, F) at 1017 cm^{-1} and (iv) the asymmetric OPO bending (ν_4, F) at 567 cm^{-1}.

In molecular crystals, such as hydroxylapatite, the crystalline field induces distortions in the perfect phosphate tetrahedron. In particular, within the OHAp structure the PO_4^{3-} symmetry is reduced from T to C_6 point group. These effects activate the A_1 and E modes in the IR range and hence the PO_4^{3-} spectrum presents more than four bands originated from the doubly degenerate ν_2 and triply degenerate ν_4 and ν_3 modes. From the tables of symmetry correlation for the $P6_3$ space group, the predicted number of IR active bands is six for ν_3 and ν_4 modes, four for ν_2 and two for ν_1 modes. For the Raman spectrum, there are nine active bands for ν_3 and ν_4 modes, six for ν_2 and three for ν_1 modes. In the OHAp crystal the phosphate ion bands are blue shifted due to the interactions between the PO_4^{3-} distorted tetrahedron and the crystalline framework.

In Table 2, we reported our vibrational analysis (B-symmetry modes were not considered) together with other theoretical figures obtained from a previous simulation with pseudopotentials on calcium atoms (Corno et al., 2006) and from FTIR and Raman spectroscopy (Rehman and Bonfield,

206 1997; Tsuda and Arends, 1994). In the following we discuss in details each vibrational region of the
207 simulated OHAp spectrum in comparison with the theoretical and experimental results.

208 *Symmetric OPO bending (ν_2).*

209 Simulations conducted with B3LYP and pseudopotential approximation on Ca^{2+} ions (Corno et
210 al., 2006) showed this mode in a range from 482 to 527 cm^{-1}. In the micro-Raman analysis by
211 Cuscó et al. (1998) on a synthetic OHAp sample the symmetric bending mode spanned from 400 to
212 490 cm^{-1} and two well resolved signals were found at 449 and 454 cm^{-1} by Tsuda and Arends
213 (1994) using Raman spectroscopy on OHAp powders. The IR adsorption spectra of synthesized
214 OHAp powder obtained by Zakharov et al. (2004) showed two defined peaks at 462 and 474 cm^{-1}.
215 Our symmetric OPO bending (ν_2) fell in the range 437-489 cm^{-1}, where we computed two silent
216 modes (B symmetry) and six IR/Raman active vibrations, the most intense one being at 489 cm^{-1}.

217 *Asymmetric OPO bending (ν_4).*

218 Miller et al. (2001) studied the crystallinity of synthetic OHAp by infrared micro-spectroscopy
219 and focused the attention to the $\nu_4(PO_4)$ vibrational transitions, providing a detailed analysis of this
220 spectral region. The authors found three main components at 560, 573 and 600 cm^{-1} and another
221 band at 530-540 cm^{-1}, however assigned to acidic phosphate ions (HPO_4^{2-}) impurities. Cuscó and
222 co-workers (1998) distinguished several bands between 570 and 625 cm^{-1}, while Zakharov et al.
223 (2004) found two peaks at 571 and 601 cm^{-1}. Corno et al. (2006) evaluated the ν_4 signals in the
224 range 591-663 cm^{-1}. We calculated 12 normal modes (three were silent) for the asymmetric OPO
225 bending from 566 to 633 cm^{-1}.

226 *Symmetric P-O stretching (ν_1).*

227 Experimental results reported a single intense peak for the non-degenerate symmetric P-O stretch
228 at 962 cm^{-1} both in IR (Rehman and Bonfield, 1997; Zakharov et al., 2004) and in Raman (Cuscó et
229 al., 1998) spectra. In the B3LYP simulation of Corno and co-workers (2006) four modes have been
230 computed for the ν_1 stretching, in the range between 990-993 cm^{-1}. We obtained the same four

231 modes, but at lower wavenumbers: 971 cm^{-1} (B, silent), 972 cm^{-1} (A, Raman and IR), 972 cm^{-1} (E_1,
232 Raman and IR) and 974 cm^{-1} (E_2, Raman).

233 *Asymmetric P-O stretching (ν_3).*

234 From the micro-Raman analysis of Cuscó et al. (1998) this vibrational mode spans over the 1020-
235 1095 cm^{-1} range, while Zakharov and co-workers (2004) distinguished four peaks in the IR
236 spectrum (1087, ~1072, 1046, ~1032 cm^{-1}). In our simulation 12 modes were computed for the
237 asymmetric P-O stretching (ν_3) in the spectral region between 1041-1110 cm^{-1}, with three silent
238 modes. The same modes were previously obtained by Corno and co-workers (2006), but their ν_3
239 bands spanned the 1080-1146 cm^{-1} range.

240 *Vibrations of OH groups.*

241 We observed an IR/Raman band at 636 cm^{-1} (E_1 symmetry) and the Raman signal at 724 cm^{-1} (E_2
242 symmetry), assigned to OH librations. This mode has been also observed in OHAp IR spectrum at
243 630 cm^{-1} by Zakharov et al. (2004), but the similarities with experimental results are probably due
244 to some error cancellation (see below). The hydroxyl asymmetric stretching was measured in both
245 IR and Raman spectroscopies around 3575 cm^{-1} (Cuscó et al., 1998; Rehman and Bonfield, 1997;
246 Tsuda and Arends, 1994; Zakharov et al., 2004). In the simulation of Corno and co-workers (2006),
247 this mode was at 3774 cm^{-1}, while with our method it is at 3757 cm^{-1}. When anharmonicity was
248 taken into account (see the Computational Methods section), the mode shifted to lower
249 wavenumbers, at 3603 cm^{-1} in the work of Corno et al. (2006) and at 3598 cm^{-1} in the present work.
250 The OH^- symmetric stretching is a silent mode (B-symmetry). Other modes, such as the OH
251 libration previously cited, are affected by anharmonicity but, unfortunately, the CRYSTAL code
252 allows to apply the correction only to stretching ones. For this reason, it is difficult to establish a
253 direct comparison between the calculated (with harmonic approximation) and the experimental OH
254 modes.

255 On the other hand, our simulation refers to a pure OHAp and obviously bands relative to
256 impurities such as for example HPO_4^{2-}, that may be present in experimental samples, are absent.

The comparison between our vibrational frequencies and those relative to the modelling of Corno and co-workers (2006) showed that the pseudopotential approximation on Ca^{2+} ions over-estimates the experimental frequencies, with errors in a range of 30-80 cm^{-1}. By using an all electron basis set we observed a systematic deviation between the data (Figure 3), typical of the use of different basis set. This effect reduced the theoretical/experimental deviation to 15-35 cm^{-1}, obtaining a better agreement with the FTIR and Raman data of Cuscó et al. (1998), Miller et al. (2001), Rehman and Bonfield (1997), Tsuda and Arends (1994) and Zakharov et al. (2004).

Type A1 carbonated apatite

Because the optimized CAp cell does not have internal symmetry (space group *P1*), the 132 degrees of freedom are assignable only to the A (total-symmetric) irreducible representation:

$$\Gamma_{total} = 132A$$

This means that all the phosphate and lattice B- and E_2-symmetry modes observed for hydroxylapatite are now IR active. E_1 and E_2 modes gave doublets because they lost their degeneracy. These reasons explain the more complexity of the type A1 CAp spectrum presented in Figure 4, when compared to the OHAp one.

We reported in table 3 the results obtained from our simulated IR analysis alongside the experimental ones. As many calculations in the past were adopting a pseudopotential on the Ca ions (Corno et al., 2006; Ulian et al., 2012) we compare them with the present all-electron results for the Cap A1 model.

The phosphate signals are almost unaffected by the different basis set, with shifts in the order of magnitude of experimental error. The differences arise on the carbonate ion normal modes because of its interaction with calcium ions.

In the following, the vibrational analysis of the type A1 CAp structure is focused on the all-electron basis set results and divided in two subsections: in the first one we discussed mainly the phosphate ions modes; in the second one on the carbonate ion signals.

283 *Phosphate ions vibrations (1200-500 cm^{-1}).*

284 The symmetric phosphate OPO bending modes ν_2 usually give faint bands in the experimental IR
285 spectra. Petra and co-workers (2005) found one signal at 470 cm^{-1}, while Rehman and Bonfield
286 (1997) distinguished one peak at 469 cm^{-1}. In our simulation we obtained 12 normal modes between
287 421-498 cm^{-1}, with the most intense peak at 472 cm^{-1}.

288 According to the work of Kolmas et al. (2011), the asymmetric OPO ν_4 bendings fall in the range
289 562-630 cm^{-1}, where six bands have been decomposed and assigned in the following way: three are
290 originated from apatite PO_4^{3-} at 562-566, 573-585 and 601-605 cm^{-1}; one was found at 616-623 cm^{-1}
291 and was assigned to a poorly crystalline phosphate ion environment; the peak at 536-550 cm^{-1} was
292 due to HPO_4^{2-} impurities and the signal at 630 cm^{-1} was assigned to an OH libration mode. Petra et
293 al. (2005) individuated two main bands near 604 and 565 cm^{-1} and a shoulder at 575 cm^{-1}, while
294 Costa and co-workers (2012) distinguished two peaks at 600 and 560 cm^{-1}. In the work of Rehman
295 and Bonfield (1997) a band was found at 603 cm^{-1}.

296 We computed 18 normal modes for the asymmetric OPO bending in the range 562-633 cm^{-1} with
297 four intense signals at 562, 579, 586 and 610 cm^{-1}. The normal mode at 633 cm^{-1} is the same
298 observed in OHAp (ν_4 + OH libration), but with lower intensity because of the absence of the
299 hydroxyl groups contribution in the CAp model. This effect was observed also by Kolmas et al.
300 (2011), where the area of the peak at 630 cm^{-1} was seen reduced from the OHAp sample to the
301 COHAp one.

302 The symmetric P-O stretching (ν_1) presented a single peak at 961 cm^{-1} in the FTIR spectra
303 obtained by Rehman and Bonfield (1997) and Petra et al. (2005), while it was at 960 cm^{-1} in the
304 work of Kolmas and co-workers (2011) and Costa et al. (2012). In our simulation we obtained six
305 overlapped modes of weak intensities in the range 956-967 cm^{-1}.

306 The asymmetric P-O stretching (ν_3) band fell in the 1020-1110 cm^{-1} range in the micro-FTIR
307 analysis of Petra and co-workers (2005), who measured a maximum near 1030 cm^{-1} and strong
308 signals at 1045, 1064 and 1110 cm^{-1}. Two maxima were found at ca. 1033 and 1090 cm^{-1} by

Kolmas et al. (2011), while a single intense peak was observed at 1041 cm^{-1} by Rehman and Bonfield (1997) and at 1020 cm^{-1} by Costa et al. (2012). In the spectra presented in this work, we calculated the ν_3 modes in the 1149-1014 cm^{-1} region, where we computed 18 normal modes. The relative intensity of the peaks are very similar to those obtained for the OHAp structure. The strongest signal in the pure hydroxylapatite model (ν_3 at 1045 cm^{-1}, E_1 symmetry) divided in two peaks at 1047 and 1026 cm^{-1} in the type A1 CAp spectrum.

In general, the $CO_3^{2-}/2OH^-$ substitution did not shifted significantly the phosphate ion vibrational modes (only ~15 cm^{-1}) and, despite the presence of more signals, the overall shape of the spectra is almost unchanged.

Carbonate ion vibrations.

The free CO_3^{2-} has four modes: bending in plane (ν_4, *E'* symmetry), bending out-of-plane (ν_2, *A''* symmetry), symmetric stretching (ν_1, A'_1 symmetry) and asymmetric stretching (ν_3, *E'* symmetry). In the free ion spectra, the only absent signal is the one relative to the symmetric stretching, because this mode does not cause dipole variations.

When the carbonate ion was placed in the apatite lattice, the *E'* modes (ν_3 and ν_4) lost their degeneracy because of the symmetry lowering and gave origin to two doublets.

The characteristic signal that evidences the carbonate ion presence in the apatite cell is the asymmetric C-O stretching (ν_3), whose doublet usually falls between 1400 and 1600 cm^{-1}. Detailed experimental vibrational analysis of the type A1 carbonate ion was provided by Fleet and Liu (2003), who measured the FTIR spectrum of a carbonate-rich carbonated apatite of composition 0.75CAp·0.25OHAp, with negligible amount of type B carbonate ion. The CO_3^{2-} ν_3 mode gave two peaks at 1461 and 1544 cm^{-1}. In the infra-red spectrum of the carbonated hydroxylapatite (COHAp) obtained by Rehman and Bonfield (1997) these signals are at 1470 and 1650 cm^{-1}, while they were found at 1458 and 1538 cm^{-1} in the Mg-COHAp sample of Kolmas and co-workers (2011). In two other experimental studies, a single peak was found at 1430 (Costa et al., 2012) and 1461 cm^{-1}

(Petra et al., 2005) for a COHAp coating and for a bone sample treated with acetone to remove the organic phase, respectively. In an earlier theoretical work on static-lattice carbonated apatite (Peeters et al., 1997), the ν_3 mode was found at 1720 and 1332 cm^{-1}. We calculated the asymmetric C-O stretching doublet at 1518 and 1604 cm^{-1}, which is blue shifted by about 55 cm^{-1} if compared to the experimental results. Using pseudopotential on Ca ions, the ν_3 signals were at 1555 and 1681 cm^{-1}, i.e. the all-electron basis set improved substantially the agreement of this bands with respect to experiment.

The out-of-plane bending mode (ν_2) is commonly used to evaluate the proportion of type A and B carbonate ion amount in the sample, because it falls at slightly different frequencies according to the site occupied by the carbonate (Fleet, 2009). For type A carbonate ion ν_2 has been found at 878 cm^{-1} (Costa et al., 2012; Fleet and Liu, 2003; Fleet et al., 2011; Kolmas et al., 2012; Petra et al., 2005), 873 cm^{-1} (Rehman and Bonfield, 1997) and at 871 cm^{-1} (Kolmas et al., 2011). In the work of Peeters and co-workers (1997) this mode was computed at 880 cm^{-1}, while in our simulated IR spectrum it is at 878 cm^{-1} and at 900 cm^{-1} with all electron and pseudo potential basis sets, respectively, again showing a slight improvement with respect to experiment when the all-electron basis set is adopted for the Ca ions .

The OCO bending mode (ν_4) was measured at 650 and 750 cm^{-1} by Petra et al. (2005) and was calculated at 541 and 808 cm^{-1} by Peeters and co-workers (1997). We obtained two very weak peaks at 670 and 781 cm^{-1} with all electron basis set, while they were at 694 and 827 cm^{-1} with the pseudopotential on Ca ions, showing a better agreement to experiment when adopting the all-electron basis set for Ca ions .

In addition, we observed a weak signal related to the symmetric stretching of the carbonate ion (ν_1) at 1134 cm^{-1} (and 1140 cm^{-1} with pseudopotential on Ca atoms). In high-symmetric structures where the carbonate ion is placed in a similar environment, *i.e.* calcite and aragonite, this vibrational mode is visible only by Raman spectroscopy. Because of the interaction with the apatite

lattice, the $\nu_1(CO_3)$ mode was active in IR, although its related signal has very low intensity and it is not clearly visible in Figure 3. It appears as a small shoulder on the $\nu_3(PO_4)$ band. The same result was obtained by Peeters and co-workers (1997) in their static-lattice model of carbonated apatite, but the symmetric stretching was calculated at 1043 cm^{-1}. We have not found any experimental evidence of this observation, probably because of the weak intensity of the carbonate ion symmetric stretching mode and the overlapping of the peak with the HPO_4^{2-} impurity bands commonly found in both synthetic and natural samples.

Compared to the "free" CO_3^{2-}, the type A1 carbonate ion establishes significant interactions with the surrounding calcium ions of the apatite channel. This is reflected in the amplitude of the IR shifts, especially for the high -frequency modes (ν_3 and ν_1).

Our carbonated apatite model refers to a perfectly periodic type A1 CAp end-member, with a CO_3^{2-} ion content fixed at 5.8 wt.%. It is not possible to make a direct peak-to-peak comparison between simulated and experimental spectra because the experimentally analyzed carbonated apatite samples may vary in composition because obtained from different sources, synthesis processes, type of minerals and also bone tissues. In the experimentally analyzed samples the carbonate ion amount may range between 1-12 wt.%, because of the possible simultaneous presence of type A and type B carbonate ions in the apatite cell. Usually there are hydroxyl groups, the presence of other ionic substitutions, *i.e.* Mg^{2+}/Ca^{2+} and the presence of type B CO_3^{2-} ions. The matrix effects can cause several problems in detecting weak signals, especially in bone samples.

However, the results that we obtained from the simulated IR spectra are in good agreement with the FTIR data reported in literature. Better accordance was found for the phosphate ion normal modes, with an average difference of 10 cm^{-1}. Considering the carbonate ion, the computed ν_2 mode matches perfectly with experimental results, with deviations in the order of magnitude of the instrumental resolution (ca. 5 cm^{-1}). The most evident discordance was obtained for the carbonate ion asymmetric stretching mode (ν_3): our simulation gave the doublet blue shifted of about 50 cm^{-1} compared to the FTIR results. However, we observed that the separation between the two peaks (86

385 cm^{-1} in our spectrum) is in good agreement with the ones of Fleet and Liu (2003) and Kolmas et al.
386 (2011), that are 83 and 80 cm^{-1}, respectively. This deviation is imputable to the different
387 composition of the modelled structure (a CAp end-member) and the experimental samples
388 (synthetic and natural).
389
390 **Type A2 and planar carbonated apatite**
391 We have reported in our previous work that the type A2 configuration, with a bisector of the
392 CO_3^{2-} triangular plane parallel to the *c*-axis, is not energetically favourable and the carbonate ion
393 rotated in the channel to reach the type A1 configuration (Ulian et al., 2012). For this reason, it was
394 not possible to obtain a vibrational spectra of the type A2 CO_3^{2-} ion in the cell.
395 On the other hand, it was found that the planar configuration, with the CO_3^{2-} molecular plane
396 perpendicular to the *c*-axis, represents a stationary point on the potential energy surface. This
397 structure was geometrically optimized with the same computational parameters, with and without
398 symmetry (space groups *P3* and *P1*, respectively). The graphical results are reported in Figure 5.
399 Despite the geometry results, the electronic energy of the planar configuration was really high if
400 compared to the A1 configuration (+165.78 kJ/mol and +164.78 kJ/mol for the *P3* and *P1* structure,
401 respectively).
402 Then, to better understand the nature of this stationary point, we also evaluated the vibrational
403 spectra of the planar CAp, with both *P1* and *P3* symmetries, obtaining two imaginary frequencies at
404 -35 cm^{-1} and -59 cm^{-1}, respectively. These results are not surprising for such high-energy structures:
405 the planar configuration is phononically instable at Γ point and then it is a saddle point on the
406 potential energy surface. The latter statement is justified by the analysis of the modes with
407 imaginary frequency, because they are related to rotations of the plane of the CO_3^{2-} that bring the
408 molecule into the A1 configuration. We excluded calculation artefacts, because of the very good
409 convergence criteria, the high number of *k* sampling points and because the vibrational analysis was
410 performed with and without symmetry constraints.

411
412
413
414 **REFERENCES CITED**
415
416 Astala, R., and Stott, M.J. (2005) First principles investigation of mineral component of bone: CO_3
417 substitutions in hydroxyapatite. Chemistry of Materials, 17(16), 4125-4133.
418 Becke, A.D. (1993) Density-Functional Thermochemistry .3. The Role of Exact Exchange. Journal of
419 Chemical Physics, 98(7), 5648-5652.
420 Bertinetti, L., Tampieri, A., Landi, E., Ducati, C., Midgley, P.A., Coluccia, S., and Martra, G. (2007) Surface
421 structure, hydration, and cationic sites of nanohydroxyapatite: UHR-TEM, IR, and microgravimetric
422 studies. Journal of Physical Chemistry C, 111, 4027-4035.
423 Corno, M., Busco, C., Civalleri, B., and Ugliengo, P. (2006) Periodic ab initio study of structural and
424 vibrational features of hexagonal hydroxyapatite $Ca_{10}(PO_4)_6(OH)_2$. Phys. Chem. Chem. Phys., 8,
425 2464-2472.
426 Costa, D.O., Allo, B.A., Kalassen, R., Hutter, J.L., Dixon, S.J., and Rizkalla, A.S. (2012) Control of surface
427 topography in biomimetic calcium phosphate coatings. Langmuir, 28, 3871-3880.
428 Cuscó, R., Guitian, F., de Aza, S., and Artus, L. (1998) Differentiation between hydroxyapatite and beta-
429 tricalcium phosphate by means of mu-raman spectroscopy. Journal of the European Ceramic
430 Society, 18(9), 1301-1305.
431 Dorozhkin, S.V. (2009) Calcium Orthophosphates in Nature, Biology and Medicine. Materials, 2, 399-398.
432 -. (2010) Bioceramics of calcium orthophosphates. Biomaterials, 31, 1465-1485.
433 Dovesi, R., Roetti, C., Freyria Fava, C., Prencipe, M., and Saunders, V.R. (1991) On the elastic properties of
434 lithium, sodium an potassium oxide. An ab initio study. Chemical Physics, 156, 11-19.
435 Dovesi, R., Saunders, V.R., Roetti, C., Orlando, R., Zicovich-Wilson, C.M., Pascale, F., Civalleri, B., Doll,
436 K., Harrison, N.M., Bush, I.J., D'Arco, P., and Llunell, M. (2009) CRYSTAL09 User's Manual.
437 University of Torino, Torino.
438 Elliott, J.C. (1998) Recent studies of apatites and other calcium orthophosphates. In E. Brès, and P.
439 Hardouin, Eds. Les matériaux en phosphate de calcium. Aspects fondamentaux, p. 25-66. Sauramps
440 Medical, Montpellier.
441 Fleet, M.E. (2009) Infrared spectra of carbonate apatites: n2-Region bands. Biomaterials, 30, 1473-1481.
442 Fleet, M.E., and Liu, X. (2007) Coupled substitution of type A and B carbonate in sodium-bearing apatite.
443 Biomaterials, 28(6), 916-926.
444 -. (2008) Type A-B carbonate chlorapatite synthesized at high pressure. Journal of Solid State Chemistry,
445 181(9), 2494-2500.
446 Fleet, M.E., and Liu, X.Y. (2003) Carbonate apatite type A synthesized at high pressure: new space group
447 (P(3)over-bar) and orientation of channel carbonate ion. Journal of Solid State Chemistry, 174(2),
448 412-417.
449 -. (2004) Location of type B carbonate ion in type A-B carbonate apatite synthesized at high pressure.
450 Journal of Solid State Chemistry, 177(9), 3174-3182.
451 Fleet, M.E., Liu, X.Y., and King, P.L. (2004) Accommodation of the carbonate ion in apatite: An FTIR and
452 X-ray structure study of crystals synthesized at 2-4 GPa. American Mineralogist, 89(10), 1422-1432.
453 Fleet, M.E., Liu, X.Y., and Liu, X. (2011) Orientation of channel carbonate ions in apatite: Effect of pressure
454 and composition. American Mineralogist, 96(7), 1148-1157.
455 Hughes, J.M., and Rakovan, J. (2002) The crystal structure of apatite, $Ca_5(PO_4)_3(F,OH,Cl)$. In M.J. Kohn, J.
456 Rakovan, and J.M. Hughes, Eds. Phosphates, 48, p. 1–12. Mineralogical Society of America,
457 Washington, D.C.
458 Kolmas, J., Jaklewicz, A., Zima, A., Bucko, M., Paszkiewicz, Z., Lis, J., Slosarczyk, A., and Kolodziejski,
459 W. (2011) Incorporation of carbonate and magnesium ions into synthetic hydroxyapatite: The effect
460 on physicochemical properties. Journal of Molecular Structure, 987(1-3), 40-50.
461 Kolmas, J., Szwaja, M., and Kolodziejski, W. (2012) Solid-state NMR and IR characterization of
462 commercial xenogenic biomaterials used as bone substitutes. Journal of Pharmaceutical and
463 Biomedical Analysis, 61, 136-141.
464 Kovaleva, E.S., Shabanov, M.P., Putlyaev, V.I., Tretyakov, Y.D., Ivanov, V.K., and Silkin, N.I. (2009)
465 Bioresorbable carbonated hydroxyapatite $Ca_{10-x}Na_x(PO_4)_{6-x}(CO_3)_x(OH)_2$ powders for bioactive
466 materials preparation. Cent. Eur. J. Chem, 7(2), 168-174.

Lee, C.T., Yang, W.T., and Parr, R.G. (1988) Development of the Colle-Salvetti Correlation-Energy Formula into a Functional of the Electron-Density. Physical Review B, 37(2), 785-789.

Lindberg, B. (1988) A New Efficient Method for Calculation of Energy Eigenvalues and Eigenstates of the One-Dimensional Schrodinger-Equation. Journal of Chemical Physics, 88(6), 3805-3810.

Miller, L.M., Vairavamurthy, V., Chance, M.R., Mendelsohn, R., Paschalis, E.P., Betts, F., and Boskey, A.L. (2001) In situ analysis of mineral content and crystallinity in bone using infrared micro-spectroscopy of the v(4) PO43- vibration. Biochimica Et Biophysica Acta-General Subjects, 1527(1-2), 11-19.

Momma, K., and Izumi, F. (2008) VESTA: a three-dimensional visualization system for electronic and structural analysis. J. Appl. Crystallogr., 41, 653-658.

Monkhorst, H.J., and Pack, J.D. (1976) Phys. Rev. B, 8, 5188-5192.

Pascale, F., Zicovich-Wilson, C.M., Gejo, F.L., Civalleri, B., Orlando, R., and Dovesi, R. (2004) The calculation of the vibrational frequencies of crystalline compounds and its implementation in the CRYSTAL code. Journal of Computational Chemistry, 25(6), 888-897.

Peeters, A., DeMaeyer, E.A.P., VanAlsenoy, C., and Verbeeck, R.M.H. (1997) Solids modeled by ab initio crystal-field methods .12. Structure, orientation, and position of A-type carbonate in a hydroxyapatite lattice. Journal of Physical Chemistry B, 101(20), 3995-3998.

Peroos, S., Du, Z., and de Leeuw, N.H. (2006) A computer modelling study of the uptake, structure and distribution of carbonate defects in hydroxy-apatite. Biomaterials, 27, 2150-2161.

Petra, M., Anastassopopulou, J., Theologis, T., and Theophanides, T. (2005) Synchrotron mirco-FT-IR spectroscopic evaluation of normal paediatric human bone. J Mol Struct, 733, 101-110.

Prencipe, M., Pascale, F., Zicovich-Wilson, C.M., Saunders, V.R., Orlando, R., and Dovesi, R. (2004) The vibrational spectrum of calcite (CaCO3): an ab initio quantum-mechanical calculation. Physics and Chemistry of Minerals, 31(8), 559-564.

Rehman, I., and Bonfield, W. (1997) Characterization of hydroxyapatite and carbonated apatite by photo acoustic FTIR spectroscopy. Journal of Materials Science-Materials in Medicine, 8(1), 1-4.

Sturgeon, J.L., and Brown, P.W. (2009) Effects of carbonate on hydroxyapatite formed from $CaHPO_4$ and $Ca_4(PO_4)_2O$. j. Mater. Sci: Mater Med, 20, 1787-1794.

Suda, H., Yashima, M., Kakihana, M., and Yoshimura, M. (1995) Monoclinic <--> Hexagonal Phase Transition in Hydroxyapatite Studied by X-ray Powder Diffraction and Differential Scanning Calorimeter Techniques. Journal of Physical Chemistry, 99(17), 6752-6754.

Suetsugu, Y., Shimoya, I., and Tanaka, J. (1998) Configuration of Carbonate Ions in Apatite Structure Determined by Polarized Infrared Spectroscopy. J. Am. Ceram. Soc., 81, 746-748.

Tosoni, S., Pascale, F., Ugliengo, P., Orlando, R., Saunders, V.R., and Dovesi, R. (2005) Quantum mechanical calculation of the OH vibrational frequency in crystalline solids. Molecular Physics, 103(18), 2549-2558.

Tsuda, H., and Arends, J. (1994) Orientational micro-Raman spectroscopy on hydroxyapatite single crystals and human enamel crystallites. Journal of Dental Research, 73, 1703-1710.

Ugliengo, P. (2009) MOLDRAW: A molecular graphics program to display and manipulate molecular structures, H1 (32-bit).

Ugliengo, P., Pascale, F., Merawa, M., Labeguerie, P., Tosoni, S., and Dovesi, R. (2004) Infrared spectra of hydrogen-bonded ionic crystals: Ab initio study of Mg(OH)(2) and beta-Be(OH)(2). Journal of Physical Chemistry B, 108(36), 13632-13637.

Ulian, G., Valdrè, G., Corno, M., and Ugliengo, P. (2012) Periodic ab initio bulk investigation of hydroxylapatite and type A carbonated apatite with both pseudopotential and all electron basis sets for calcium atoms. American Mineralogist, Accepted.

Valenzano, L., Noel, Y., Orlando, R., Zicovich-Wilson, C.M., Ferrero, M., and Dovesi, R. (2007) Ab initio vibrational spectra and dielectric properties of carbonates: magnesite, calcite and dolomite. Theoretical Chemistry Accounts, 117(5-6), 991-1000.

Valenzano, L., Torres, F.J., Klaus, D., Pascale, F., Zicovich-Wilson, C.M., and Dovesi, R. (2006) Ab initio study of the vibrational spectrum and related properties of crystalline compounds; the case of CaCO3 calcite. Zeitschrift Fur Physikalische Chemie-International Journal of Research in Physical Chemistry & Chemical Physics, 220(7), 893-912.

Zakharov, N.A., Polunina, I.A., Polunin, K.E., Rakitina, N.M., Kochetkova, E.I., Sokolova, N.P., and Kalinnikov, V.T. (2004) Calcium hydroxyapatite for medical applications. Inorganic Materials, 40(6), 641-648.

525

Table 1. B3LYP lattice parameters and mean geometric characteristics of initial models

	OHAp*	**CAp***
Symmetry	$P6_3$	P1
a (Å)	9.433	9.582
b (Å)	9.433	9.764
c (Å)	6.896	6.877
α (°)	90.0	89.3
β (°)	90.0	89.8
γ (°)	120.0	121.9
V_{cc} (Å^3)	532	546
Mean bond length (Å)		
P – O	1.55	1.54
O – H	0.97	-
C – O	-	1.29
Ca --- O (*c*-channel)	2.37	2.36
Mean bond angle (°)		
O – P – O	109.4	110.1
O – C – O	-	120.0

Notes: V_{cc} is the volume of the crystallographic cell. O (*c*-channel) refers to an oxygen atom of hydroxyl group and in OHAp cell or carbonate ion in type A1 CAp structure.
* (Ulian and Valdrè, 2012)

526
527
528
529
530
531
532
533
534
535
536
537
538
539
540
541
542
543
544
545
546
547
548

Table 2. Harmonic frequencies for the B3LYP-simulated OHAp bulk structure.

			Calculated			Experimental		
Mode	**Symmetry**	**Active**	**B3LYP***	**Ampl. (IR)***	**B3LYP§**	**IR◊**	**Raman‡**	**Δν**
ν_2 (PO4)	A	IR, R	459	0.2	506		432	+27
	A	IR, R	489	40.4	527		454	+35
	E_1	IR, R	437	2.4	476			
	E_1	IR, R	475	34.6	515		432	+43
	E_2	R	440	0	482	462	449	-9
	E_2	R	457	0	515			
ν_4 (PO4)	A	IR, R	566	1095.5	599	566		
	A	IR, R	599	0.1	630	660-520	593	+6
	A	IR, R	621	4.2	656		609	+12
	E_1	IR, R	573	691.2	602			
	E_1	IR, R	600	166.7	632	632		
	E_1	IR, R	609	735.2	639	602		
	E_2	R	566	0	591		581	-15
	E_2	R	588	0	622		609	-21
	E_2	R	633	0	663		617	+16
ν_1 (PO4)	A	IR, R	972	2.62	991		962	+10
	E_1	IR, R	972	360.2	990	962		
	E_2	R	974	0	993		962	+12
ν_3 (PO4)	A	IR, R	1054	4686.4	1088	1190-976	1034	+20
	A	IR, R	1064	136.6	1111		1048	+16
	A	IR, R	1096	1.0	1127		1077	+19
	E_1	IR, R	1045	8207.8	1080		1043	+2
	E_1	IR, R	1068	97.6	1107	1042		
	E_1	IR, R	1110	755.8	1146	1091		
	E_2	R	1041	0	1081		1028	+13
	E_2	R	1077	0	1109		1055	+22
	E_2	R	1081	0	1126		1077	+4
ν $(OH)_{harm}$	A	IR, R	3757	-	3774			
ν $(OH)_{anharm}$	A	IR, R	3598	88.0	3603	3573	3572	+26

Notes: Ampl. (IR) is the calculated infrared transition amplitude. Δν has been evaluated from Raman spectroscopy.
* present work
§ (Corno et al., 2006)
◊ (Rehman and Bonfield, 1997)
‡ (Tsuda and Arends, 1994)

Table 3. Harmonic frequencies for the B3LYP-simulated CAp bulk structure.

	B3LYP*		FTIR (experimental)			$\Delta\nu_{(CAp-FTIR)}$		
Mode	**OHAp**	**CAp**	**(a)**	**(b)**	**(c)**	**(a)**	**(b)**	**(c)**
ν_2 (PO_4)	475	471	469	470	-	+2	+1	-
ν_4 (PO_4)	566	562	-	564	566	-	-2	-4
	588	586	-	575	580	-	+11	+6
	609	610	603	604	604	+7	+6	+6
ν_1 (PO_4)	972	961	961	961	960	0	0	+1
ν_3 (PO_4)	1045	1047	1041	1044	1033	+6	+3	+14
	1054	1064	-	1064	-	-	0	-
	1110	1110	-	1110	1090	-	0	+20
ν_{4a} (CO_3)	-	670	-	670	-	-	0	-
ν_{4b} (CO_3)	-	781	-	750	-	-	+31	-
ν_2 (CO_3)	-	878	873	878	879	+5	0	-1
ν_1 (CO_3)	-	1134	-	-	-	-	-	-
ν_{3a} (CO_3)	-	1518	1470	1461	1458	+48	+57	+60
ν_{3b} (CO_3)	-	1604	1650	-	1538	-46	-	+66

Notes: All the frequencies are in wavenumbers (cm^{-1}). The results of the present work (*) are reported alongside the FTIR analysis of (a) Reman and Bonfield (1997), (b) Petra et al. (2005) and (c) Kolmas et al. (2011), respectively.

Figure 1. Optimized hydroxyl- (a) and carbonated apatite (b) crystallographic cell obtained from *ab initio* simulation (Ulian and Valdrè, 2012), viewed along different directions.

Figure 2. OHAp IR vibrational spectra, where the asymmetric (ν_3) and symmetric (ν_1) stretching and the asymmetric (ν_4) and symmetric (ν_2) bending modes of phosphate group are marked. The O-H stretching is not showed for the sake of clearness.

Figure 3. Correlation between experimental and computed vibrational frequencies using Ca-pseudopotential and all electron basis sets.

Figure 4. Simulated type A1 CAp IR vibrational spectra. Asymmetric (ν_3) and symmetric (ν_1) stretching and the out of plane (ν_2) bending modes of carbonate ion are marked. The OHAp spectrum (dashed line) is also reported to ease the comparison between the two structures.

Figure 5. Optimized type A carbonated apatite with CO_3^{2-} in planar configuration, viewed from (a) [001] and (b) [100] directions.

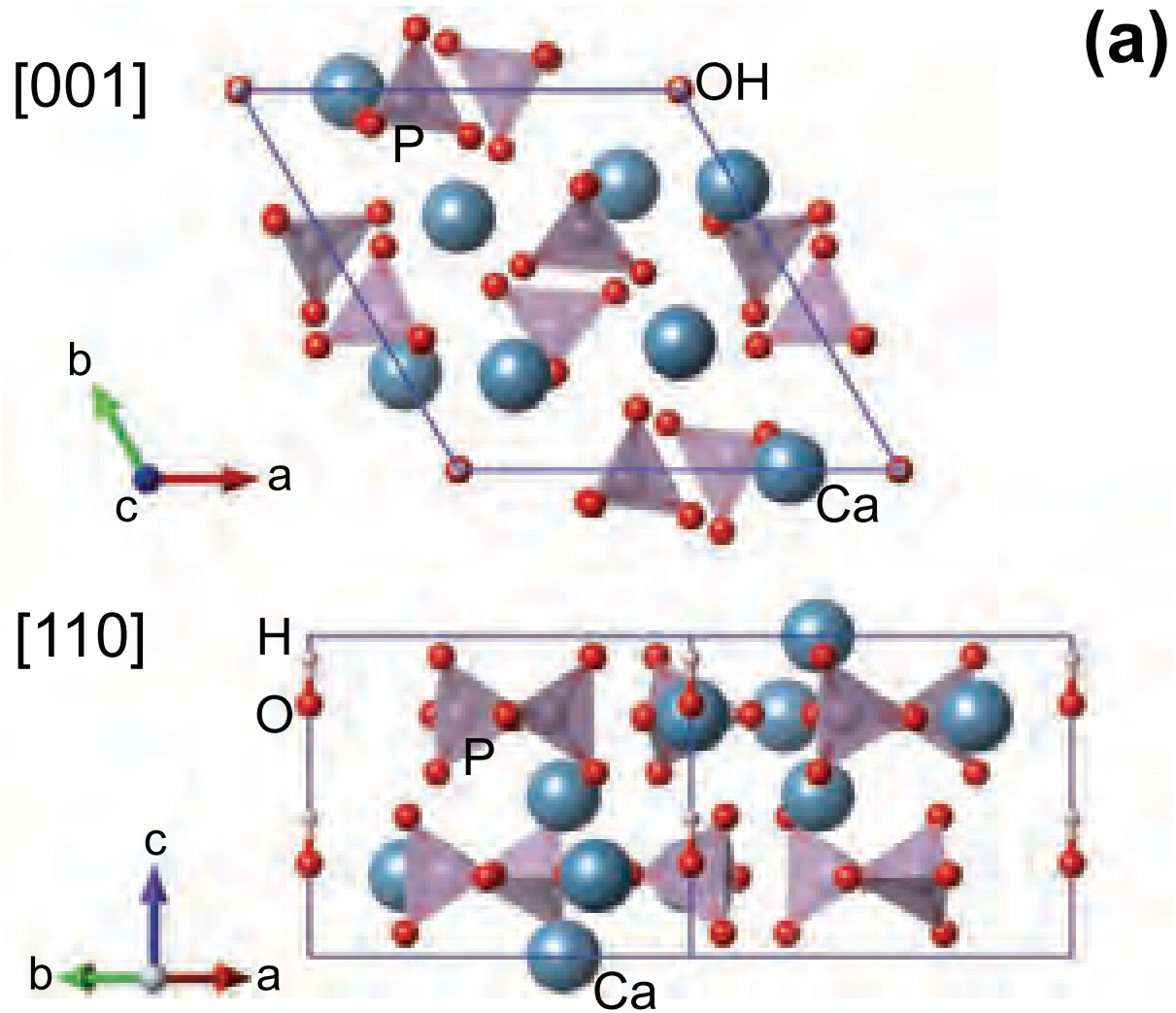
(a)
[001]
OH
P
b
a
c
Ca
[110]
H
O
P
c
b
a
Ca

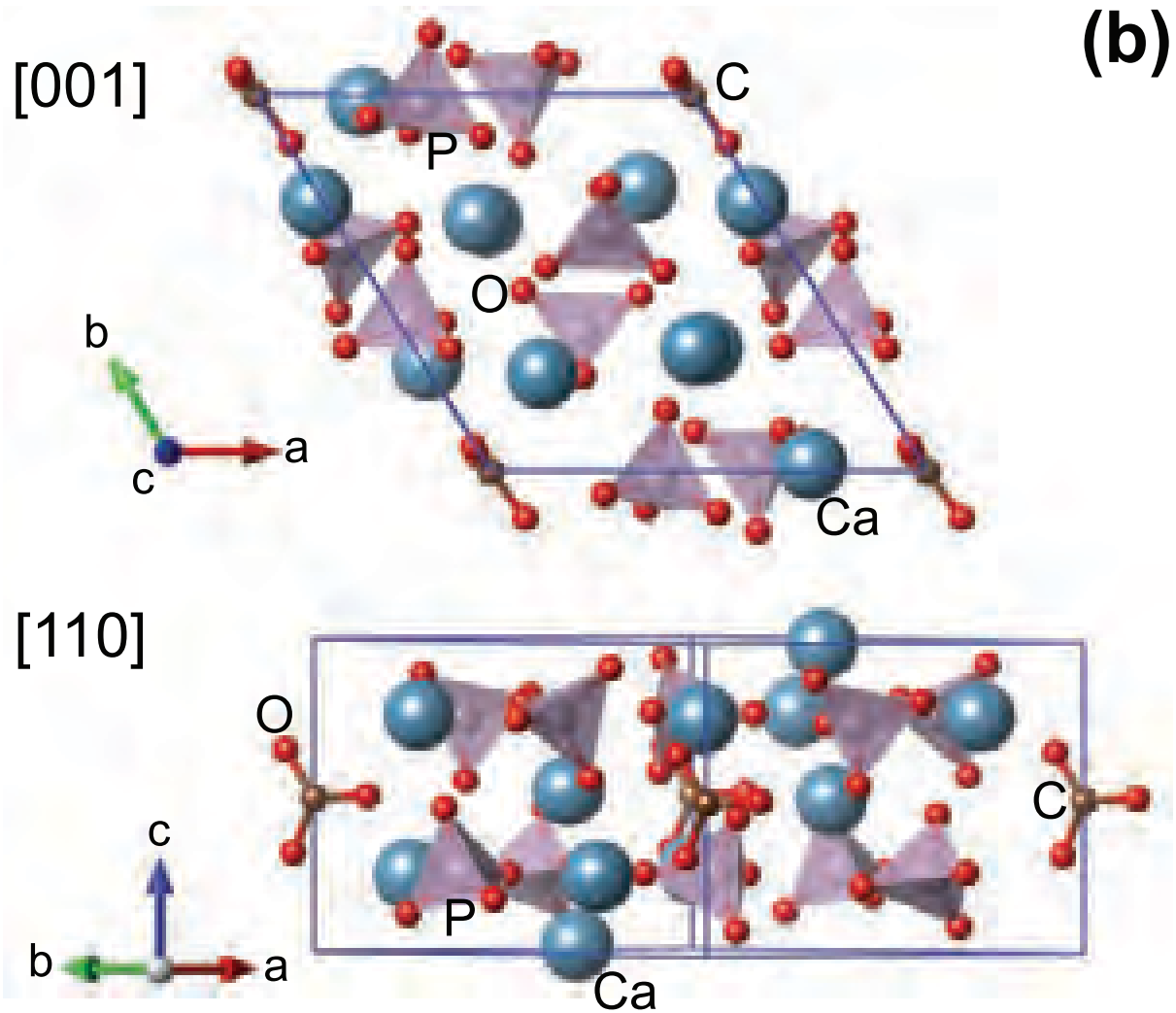
(b)
[001]
C
P
O
b
a
c
Ca
[110]
O
C
c
P
b
a
Ca

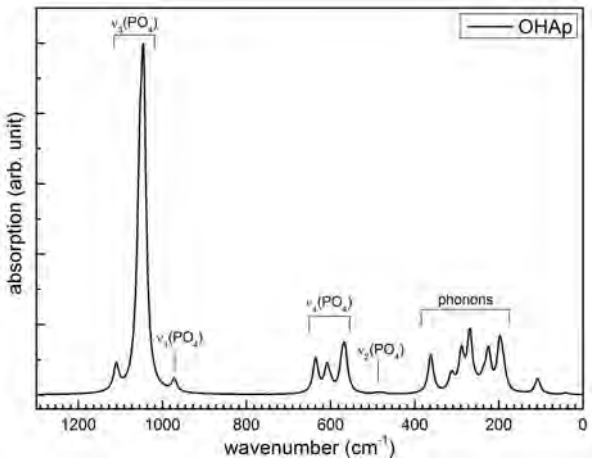
OHAp
$\nu_3(PO_4)$
$\nu_1(PO_4)$
$\nu_4(PO_4)$
$\nu_2(PO_4)$
phonons
absorption (arb. unit)
1200
1000
800
600
400
200
0
wavenumber (cm^{-1})

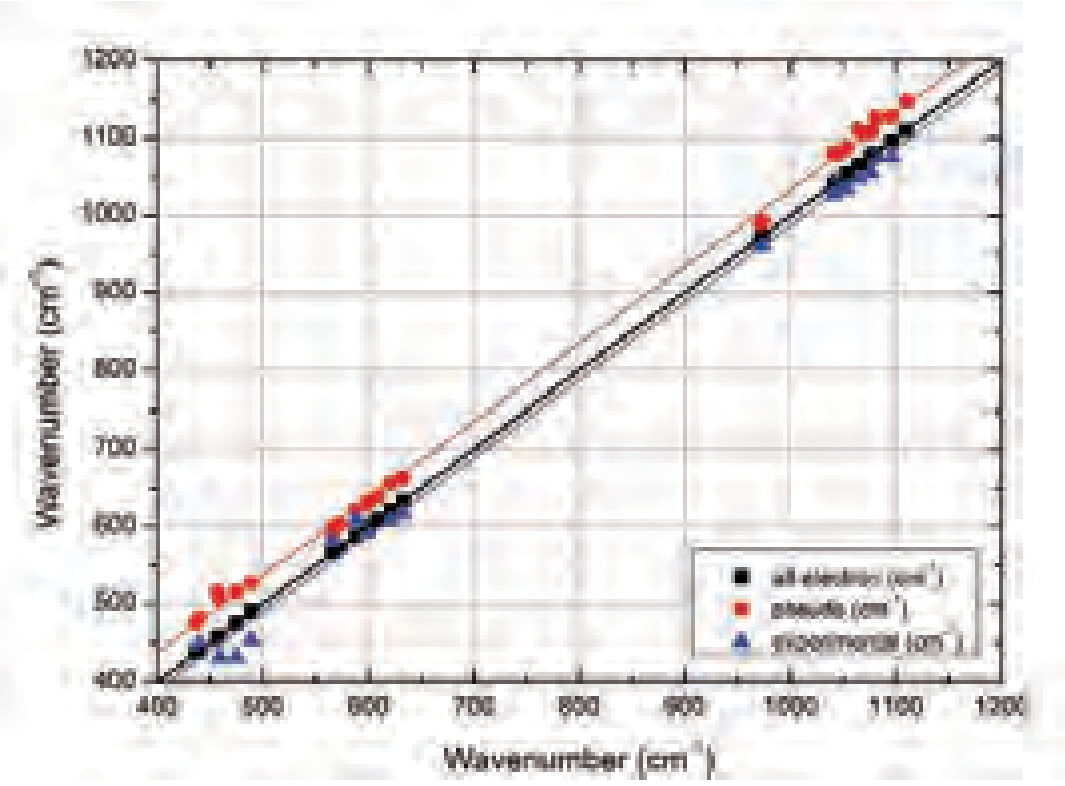
Wavenumber (cm^{-1})
Wavenumber (cm^{-1})
400
500
600
700
800
900
1000
1100
1200

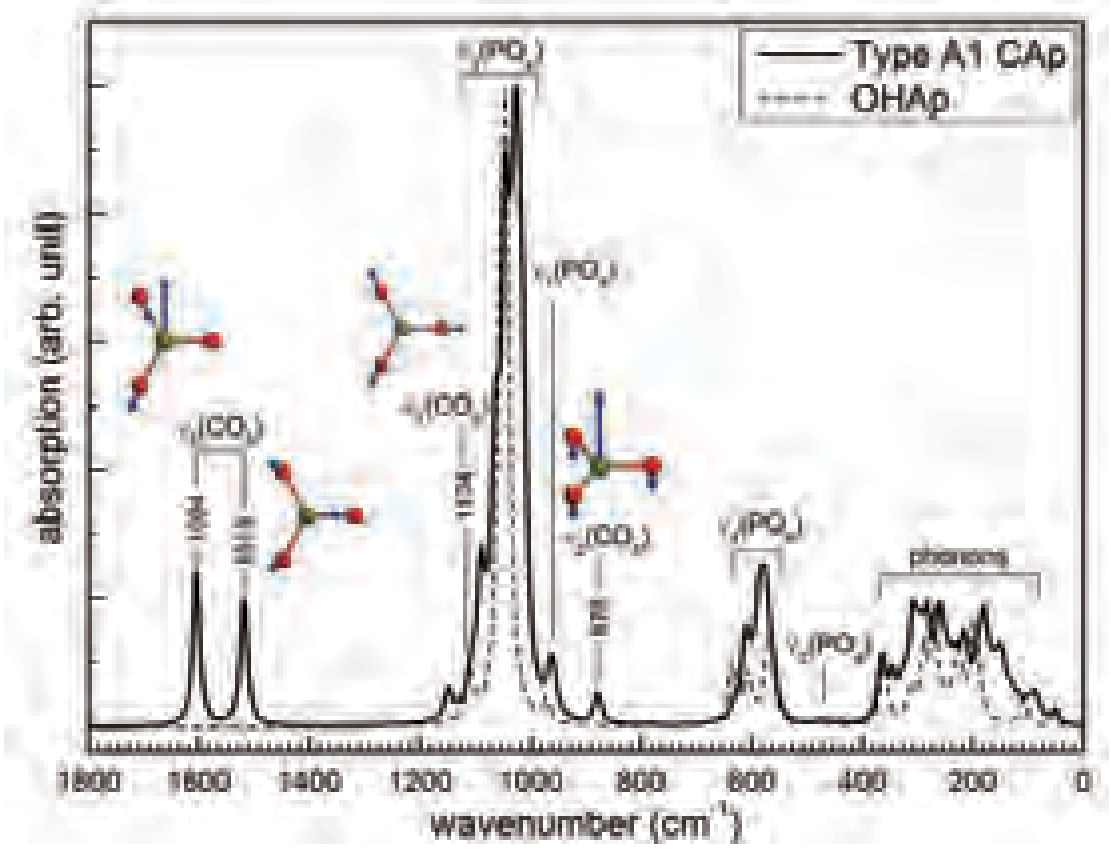
Type A1 CAp
OHAp
absorption (arb. unit)
wavenumber (cm-1)
1800
1600
1400
1200
1000
800
600
400
200
0
1454
1418
1134
879
phonons

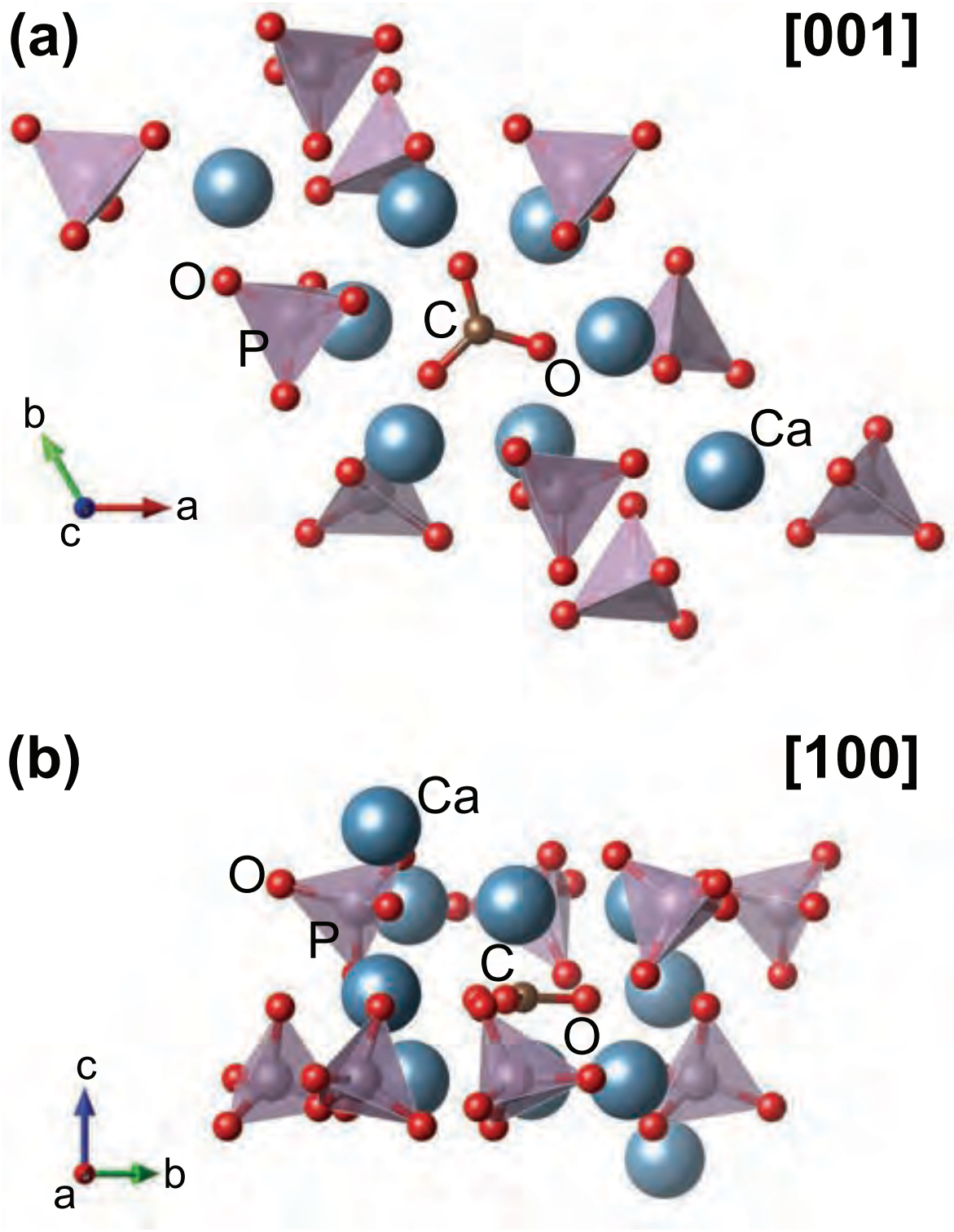
(a)
[001]
O
P
C
O
Ca
b
a
c
(b)
[100]
Ca
O
P
C
O
c
b
a